Ultra-thin Magnetic Film with Giant Phonon-drag for Heat to Spin Current Conversion

Payal Wadhwa[1], *Andrea Bosin*[1], *and Alessio Filippetti*,[1,2*]

1 Dipartimento di Fisica, Università di Cagliari. S.P. Monserrato Sestu Km.0,700. Monserrato (Ca) 09042-I, Italy
2 Consiglio Nazionale delle Ricerche, Istituto Officina dei Materiali, CNR-IOM, S.P. Monserrato Sestu Km.0,700. Monserrato (Ca) 09042-I, Italy

* Corresponding author: alessio.filippetti@dsf.unica.it

ABSTRACT

A tightly confined 2D electron gas with good carrier mobility and large spin-polarization is an essential ingredient for the implementation of spin-caloritronic conversion device technology. Here we give evidence that the $SrTiO_3/EuTiO_3/LaAlO_3$ heterostructure is a prototype material to the aim. The presence of Eu induces strong spin-polarization in the 2D electron gas spontaneously formed at the interface, and ferromagnetic order at low temperature. Furthermore, tight 2D confinement and spin-polarization can be highly enhanced upon charge depletion, in turn generating huge thermopower associated to the phonon-drag mechanism. Most importantly, the remarkable difference in the population of the two spin channels results in giant spin-polarized Seebeck effect, and in turn, giant spin voltages of mV/K order at the two ends of an applied thermal gradient. Our results represent a strong assessment to the capabilities of this interface for low-temperature spin-caloritronic applications.

KEYWORDS: *oxide interface, 2D electron gas, Seebeck coefficient, phonon-drag, spin-caloritronics, first-principles calculations*

After the groundbreaking discovery of the 2D electron gas (2DEG) presence at the $SrTiO_3/LaAlO_3$ (STO/LAO) interface,[1] a tremendous effort was spent by the community to introduce some form of magnetic order in the ultrathin mobile electron layer, to enable the interface to spintronic applications. As a matter of fact, this goal turned out to be extremely complicate. In fact, the most straightforward route to achieve magnetic dilution is through B-site substitution with spin-polarized atoms, but this typically produces dramatic effects on the Ti-derived conduction bands hosting the 2DEG, with highly detrimental consequences on the transport properties. A different strategy is introducing magnetism through A-site substitutions; an optimal choice to the aim is Eu: at bulk level, $EuTiO_3$ (ETO) is characterized by a rich phenomenology in terms of magneto-electric and magneto-structural coupling,[2–16] and is isostructural to STO with identical lattice parameter (a = 3.905 Å). Furthermore, the big Eu magnetic moments derived from the fully spin-polarized 4*f* electrons are keen to establish a substantial exchange interaction with the Ti 3*d* conduction bands, owed to strong Eu 4*f* – Ti 3*d* and Eu 5*d* – Ti 3*d* orbital couplings.[17–21] Pristine ETO is antiferromagnetic with T_N = 5.5 K,[2] but ferromagnetism (FM) with T_c ~ 8-9 K can be introduced by a variety of *n*-doping substitutions.[20,22–26] Consistently with this findings, FM order is also reported for the 2DEG present at the ETO (100) surface,[27] and, most crucially for our scopes, at the STO/ETO/LAO interface,[28–31] where ferromagnetism up to T ~8 K is observed.[28,29]

A remarkable aspect reported for *n*-doped ETO is that carrier concentration is characterized by a large spin-polarization fraction, nearing 100% at low *n*.[21,32] Our working hypothesis is that similar characteristics are displayed in 2D form by the STO/ETO/LAO heterostructure as well. A fully spin-polarized 2DEG with highly mobile carriers is instrumental to implement spin-caloritronic devices[33–36] capable to convert an applied temperature gradient into a spin voltage and a spin current. This mechanism, recently described theoretically for *n*-doped ETO,[21] can be further amplified in 2D since, due to phonon confinement, the 2DEG can develop giant phonon-drag, reaching and even overcoming the mV/K order in charge-

depletion conditions.[37–41] In what follows we show that the 2DEG spontaneously formed at the STO/ETO/LAO interface is characterized by large spin-polarization and giant phonon-drag induced thermopower of mV/K order for charge densities $n \sim 10^{13}$ cm^{-2} measured in experiment,[28-31] and that that these combined characteristics convey similarly giant spin voltages at the two ends of the applied temperature gradient.

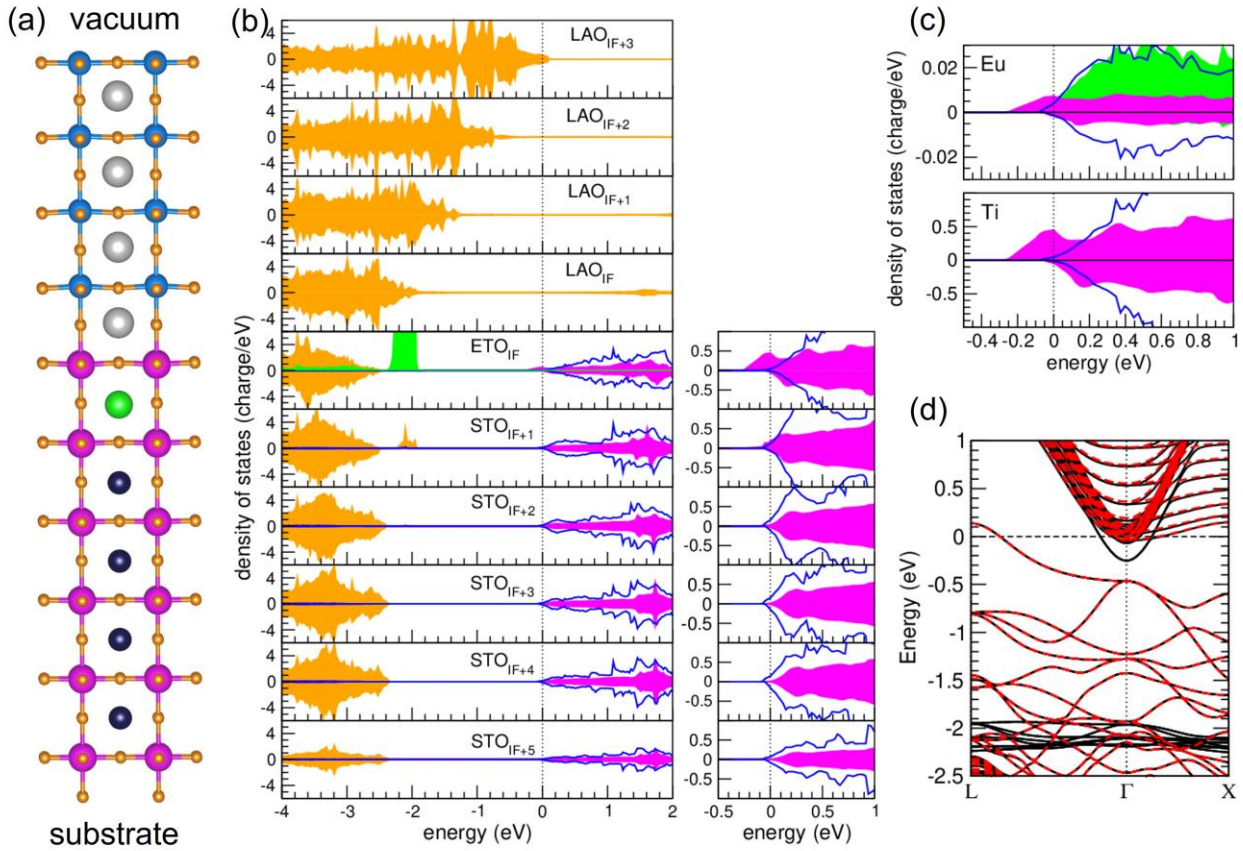

Figure 1: structural and electronic properties of the STO/ETO/LAO interface. a) atomic structure; color code is O (orange), Ti (magenta), Sr (black), Eu (green), Al (blue), La (gray). b) layer-resolved DOS for energies around the band gap; zero energy is fixed at ε_F; positive and negative values correspond to spin-majority and spin-minority channel, respectively. Only the most important orbitals are shown: O *p* (filled orange), Ti *3d* d_{xy} (filled magenta), Ti *3d* d_{xz}, d_{yz} (blue), Eu *f* (filled green); right panels are DOS enlargements around ε_F. c) orbital-resolved DOS of Eu and Ti states in the interface layer only, put on a different scale in order to appreciate the Eu contribution. For Eu: 4*f* (filled green), *5d* d_{xy} (filled magenta), *5d* d_{xz}, d_{yz} (blue); for Ti the color code is the same as in b). d) band structure; black and red-dashed bands correspond to spin-majority and spin-minority states, respectively.

Experimentally, the 2DEG in STO/ETO/LAO is only observed for heterostructures including 1 or 2 ETO layers; for larger thickness a sharp transition to insulating behavior occurs.[28] In the following we focus on the one ETO layer case, while the 2-ETO layer case is described in

the S.I. In Figure 1 we display atomic structure and electronic properties of the $(STO)_{10.5}/(ETO)_1/(LAO)_4$/VACUUM heterostructure, calculated by GGA+U. The supercell is symmetrized with respect to the central TiO_2 layer to avoid spurious electric fields across the STO substrate and through the vacuum. Indeed, from the orbital-resolved density of states (DOS) profile in Fig.1b we can see that an electric field is present only across the polar LAO side. The layer-resolved DOS shows the presence of a tightly confined 2DEG at the interface: as a consequence of the Zener breakdown, a portion of the electron charge moves from the O *p* surface states to the Ti *3d* interface states. As in STO/LAO, the metal-insulating transition occurs for LAO thickness of at least 4 unit cells, and the 2DEG is substantially confined within the first 4-5 STO layers from the interface. A peculiar feature which sets apart this interface from the STO/LAO prototype is the evident 2DEG magnetization: the ETO layer displays a bold DOS peak of fully magnetized Eu 4*f* states centered at ~2 eV bonding energy, in agreement with photoemission measurements.[31] By exchange coupling with the Ti 3*d* states, these huge (~7 μ_B) magnetic moments convey a spin-polarization on the 2DEG as well. The 2DEG in the single ETO layer appears fully magnetized; the magnetization is marginally injected into the adjacent STO layer as well, while carriers in the inner STO layers are weakly or non-magnetic.

The mechanism of exchange coupling is better appreciated in the DOS enlargement around the Fermi energy (ε_F) for the ETO interface layer (Fig.1c): a tiny fraction of spin-split 4*f* states overlaps in both energy and space with the Ti 3*d* states of the ETO layer. Interestingly, a small spin-polarized DOS contribution to the 2DEG even comes from Eu 5*d* t_{2g} states: as observed in bulk ETO,[17,20,21] virtual 4*f* to 5*d* excitations furnish an additional coupling channel with the Ti *3d* states, owed to the large spatial overlap of Ti *3d* t_{2g} and Eu *5d* t_{2g} orbitals.

Our calculations are in qualitative agreement with previous ab-initio results[31] for the same system, albeit we obtain a 2DEG magnetization more tightly confined to the interface. The

2EG band structure is detailed in Figures 2a and 2b: two spin-polarized bands, associated with the Ti *3d* d_{xy} orbitals (hereafter d_{xy1} and d_{xy2}) respectively located on ETO and first STO layer, collect most of the 2DEG charge. In the majority manifold, the d_{xy1} and d_{xy2} band bottom lies 247 meV and 65 meV below ε_F, respectively, and their effective mass along the [100] direction is ~0.50 m_e. We can evaluate the electron charges q_i hosted in these bands by the Luttinger's relation $q_i = A_i / A_{BZ} = a^2 A_i / (2\pi)^2$, where A_i is the cross-sectional Fermi surface area of band i ; we obtain n_{xy1} = 2.7×10^{13} cm^{-2}, n_{xy2} = 0.67×10^{13} cm^{-2}. In the minority manifold, on the other hand, only the former is populated, with n_{xy1} = 0.42×10^{13} cm^{-2}; these occupancies result in spin-polarization fractions $M_i = \left(n_i^{\uparrow} - n_i^{\downarrow}\right) / n_i$ ~ 74% and 100% for the two bands, respectively.

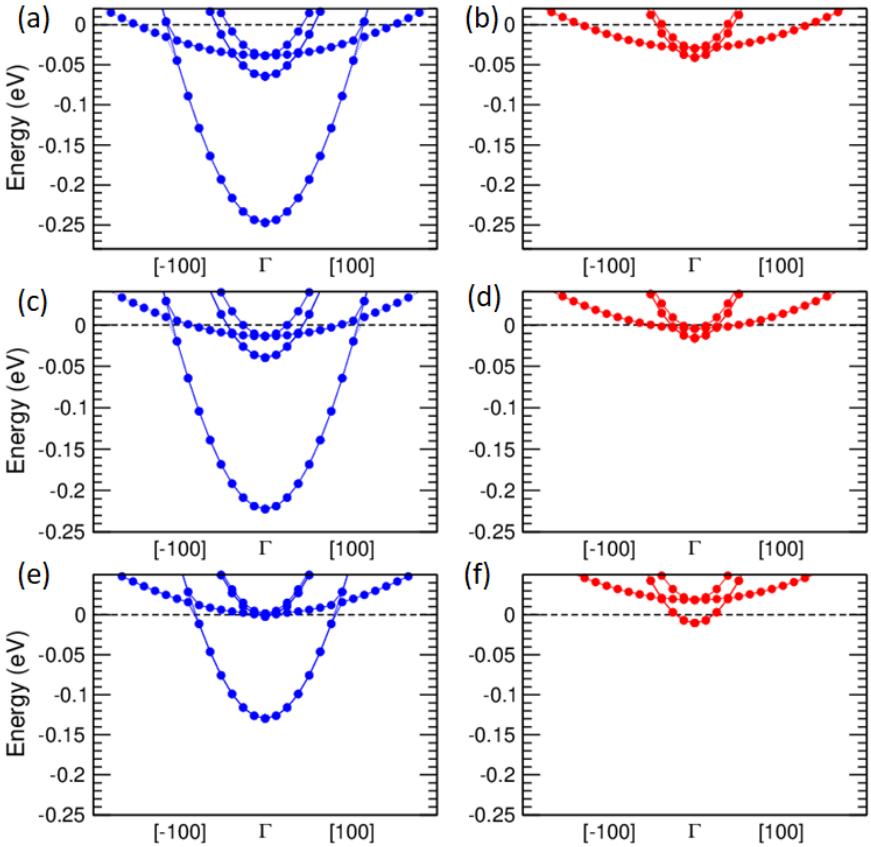

Figure 2: band structure of STO/ETO/LAO in a narrow energy window around ε_F (fixed at zero energy) within a $k \in [\pm 0.2,0,0]2\pi/a$ range. a), b): spin-majority and spin-minority bands of the STO/ETO/LAO interface with an estimated 2DEG charge density n = 8.5×10^{13} cm^{-2}. c), d): same as a) and b) but in charge depletion condition with n = 4.4×10^{13} cm^{-2}. e), f): same as above for a more depleted 2DEG with n = 1.4×10^{13} cm^{-2}.

Above in energy, we have other two occupied bands, associated to the lowest (d_{xz}, d_{yz}) orbital doublet, with masses 0.52 m_e and 5.43 m_e along [100], respectively. These states are less spatially localized than the d_{xy} states at the interface, spreading for several layers across the STO substrate; their population amounts to n = 4.7×10^{13} cm^{-2}; also, they are little spin-polarized (M_{xz} = $\underline{M_{yz}}$ = 14%) with respect to the former two. Overall, the 2DEG charge amounts to n = 8.5×10^{13} cm^{-2}, of which n = 3.8×10^{13} cm^{-2} located on the energy lowest d_{xy1} and d_{xy2} states; the 2DEG band-averaged magnetization $M = \left(n^{\uparrow} - n^{\downarrow}\right)/n$ ~ 40%.

One of the most valuable attributes of the 2DEG in oxide heterostructures is the outstanding responsivity to field effect; as well known, this allows to navigate across the phase diagram and operate the fine tuning of transport properties, such as superconductivity,[29,42] magnetoresistance,[43] Rashba effect;[44] here we are specifically interested to explore the effect of charge modulation on magnetic and thermoelectric properties. To the aim, in Figure 2 we recalculate the bands for two moderately charge-depleted states, corresponding to n = 4.4×10^{13} cm^{-2} (Figs. 2c and 2d) and n = 1.4×10^{13} cm^{-2} (Figs. 2e and 2f). These calculations are done by a supercell approach extensively used in literature,[20,45–47] which allows to overcome the limit of rigid band approximation. In depletion conditions, the more extended and less magnetized (d_{xz}, d_{yz}) bands are the first to be depopulated, so that the 2DEG becomes simultaneously more confined at the interface and more spin polarized. Indeed, M increases to 78% and 88% for the two depleted states, respectively. In particular, for the latter, d_{xy1} is the only populated band, i.e. the 2DEG is substantially confined to the single ETO layer, and almost fully spin-polarized (i.e. half-metallic).

In Figure 3 we report electric and thermoelectric transport properties of the 2DEG as a function of temperature for several charge density values; for these calculations we adopt a Bloch-Boltzmann approach within relaxation time approximation,[48,49] where the bands are described by an effective mass model, and carrier scattering is set by numerical modeling

based on ab-initio calculated parameters,[50-52] as described in the SI. We obtain mobility values similar to those typically reported for 2DEG's in oxides: as in STO/LAO, the 2DEG mobility at room-T is ruled by electron scattering with polar optical phonons, and at low-T by scattering with impurities, for which we assume a low concentration value N_{imp} = 10^{14} cm^{-3} typical of highly pure heterostructures.

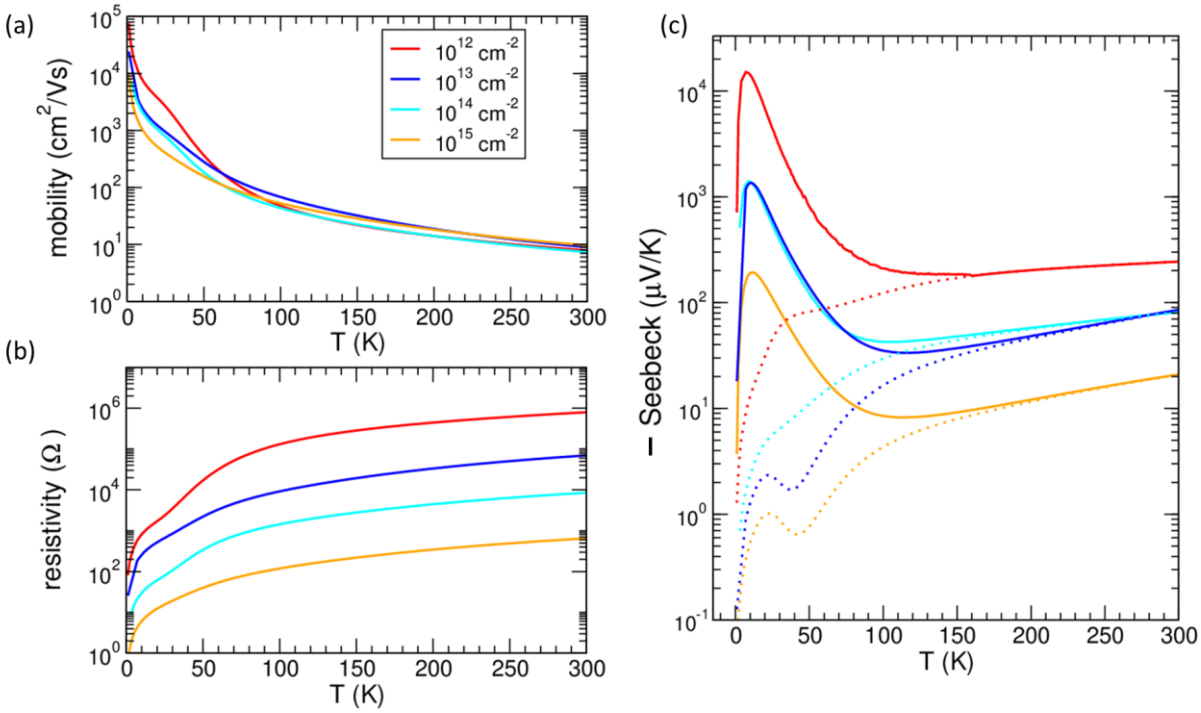

Figure 3: calculated transport properties of the STO/ETO/LaO interface vs T, for several 2D electron density values, indicated by the color legend in Figure 3a. a): mobility. b) 2D resistivity. c) (minus) the Seebeck coefficient (notice that S is negative for electrons); solid lines: total (diffusive plus phonon drag) thermopower; dotted lines: diffusive only term.

For what concerns the Seebeck (which is negative for electron carriers), at room T we obtain values ~10^2 μV/K, in line with what is reported for other oxide heterostructures.[37–41] The most remarkable aspect concerns the low-T range: if only the diffusive term is considered (as it is usually the case in calculations), the Seebeck coefficient decreases with temperature, up to vanishing at T=0. However, in response to a temperature gradient, phonons diffuse from the hot to the cold end as well; due to electron-phonon coupling, they drag the carriers, furnishing a further burst to the thermoelectric build up, the so-called phonon-drag term. The phonon drag amplitude is typically small or discardable in 3D bulk semiconductors, but it can be huge

and dominant in 2D systems, as observed in $Al_xGa_{1-x}As/GaAs$,[53] MgZnO/ZnO,[54] and STO/LAO;[37–41] in the latter, spectacular Seebeck oscillations in extreme depletion conditions were observed and attributed to phonon-drag.[40] The typical phonon-drag signature is a bold and deep peak located at $T \sim \theta_D/10$, where θ_D is the Debye temperature. We calculated the phonon-drag contribution using the theory first developed by Bailyn,[55] and then adapted by Cantrell and Butcher to 2DEG,[56] based on the Boltzmann transport equation for a system of coupled electrons and phonons (details are reported in the SI). We obtain deep phonon-drag peaks centered at $T \sim 10$ K; the phonon-drag progressively decreases with T, up to vanishing for $T \sim 150$ K; at higher T, other heat dissipation mechanisms (phonon-phonon, phonon-boundary, and phonon-impurity scattering) take place over electron-phonon scattering, thus phonon-drag becomes quenched.

The Seebeck amplitude reaches giant peak values ($S \sim$mV/K for $n = 10^{13}$ cm^{-2}, and ~10 mV/K for $n = 10^{12}$ cm^{-2}) similar to those observed in STO/LAO (e.g. S = -1.18 mV/K in a STO/LAO sample with $n = 1.7\times10^{12}$ cm^{-2}).[41] Just like in STO/LAO, the phonon-drag is dramatically enhanced by charge depletion, due to the progressive increase of 2DEG localization (a detailed analysis of localization effects of phonon-drag in STO/LAO is reported in Ref. 41). On the other hand, the peak position is substantially unaffected by the charge density. At the fundament of the 2D phonon-drag enhancement is the electron-acoustic phonon coupling: the loss of momentum conservation in the orthogonal direction allows carriers to interact with a much larger number of phonons than in the 3D analog. In fact, it can be shown that the coupling amplitude depends on the Fourier transform of the 2D-localized electron charges:[41,56]

$$F_n(q_z) = \left| \int_t dz\, \psi_n^2(z) e^{iq_z z} \right|^2 \quad (1)$$

where q_z is the phonon momentum component in the orthogonal direction z, $\psi_n^2(z)$ the planar-averaged wavefunction, and t the 2DEG thickness. Only phonon wavelengths much

longer than the wavefunction length-scale give non-vanishing contributions to the integral; thus in the delocalized limit ($t \to \infty$) only the q_z = 0 term survives, while in the localized limit ($t \to 0$) $F_n \sim 1$ for each q_z up to the Debye wavelength (more details are reported in the SI and in Ref. 41).

It emerges from our analysis that the 2D charge localization produces the simultaneous enhancement of both spin-polarization and thermopower of 2DEG; since charge localization can be efficiently controlled by field effect, the exploitation of this interface for spin-caloritronic means can be envisioned. The mechanism is schematically described in Figure 4: a substantial difference in up-spin and down-spin population reverberates in markedly different conductivity and thermopower for the two spin channels, which in turn result in large spin currents and spin voltages. In closed circuit condition (Fig.4a) the thermally generated currents for the two channels are $J_c^{\uparrow\downarrow} = -\sigma^{\uparrow\downarrow} S^{\uparrow\downarrow} \nabla T$, and the associated spin current $J_s = J_c^{\uparrow} - J_c^{\downarrow} = \left(\sigma^{\downarrow} S^{\downarrow} - \sigma^{\uparrow} S^{\downarrow}\right) \nabla T$, where $\sigma^{\uparrow\downarrow}$ and $S^{\uparrow\downarrow}$ are conductivity and Seebeck of individual spin channels, respectively, ad ∇T the applied temperature gradient. In open-circuit condition (Fig.4b) the current is blocked and a potential bias is generated at the sample ends on which ∇T is applied; by definition, the bias generated by the accumulation of spin-majority and spin-minority carriers is $\Delta V^{\uparrow\downarrow} = -S^{\uparrow\downarrow} \Delta T$, corresponding to an effective field $E^{\uparrow\downarrow} = -\nabla V^{\uparrow\downarrow} = S^{\uparrow\downarrow} \nabla T$; from the latter we see that the Seebeck coefficient corresponds to the electromotive force generated at the two ends by a unitary temperature gradient. The key point is that, while both up-spin and down-spin electrons migrate from the hot to the cold end, if the spin relaxation length is longer than the crossed channel, the respective bias and the corresponding field can be largely different, owed to the different spin-channel populations. Notice that, while the spin-majority carriers generate most of the current, ΔV is larger for spin-minority carriers (see Fig. 4b), since at low doping $S^{\uparrow,\downarrow} \sim \left(\varepsilon_F - \varepsilon_{CBB}^{\uparrow,\downarrow}\right) / eT$. It follows that

an unbalance of up-spin $\mu^{\uparrow}$ and down-spin $\mu^{\downarrow}$ chemical potentials is generated at the two ends of the thermal gradient. If $\Delta\mu^{\uparrow\downarrow} = \mu_H^{\uparrow\downarrow} - \mu_C^{\uparrow\downarrow}$ is the chemical potential disalignment between hot (H) and cold (C) end, the chemical potential spin-splitting at the two ends is:

$$\mu_H^{\uparrow} - \mu_H^{\downarrow} = \mu_C^{\downarrow} - \mu_C^{\uparrow} = \frac{1}{2}\left(\Delta\mu^{\uparrow} - \Delta\mu^{\downarrow}\right) \tag{2}$$

Since $\Delta\mu^{\uparrow\downarrow} = -e\,\Delta V^{\uparrow\downarrow} = e\,S^{\uparrow\downarrow}\,\Delta T$, we have:

$$\mu_H^{\uparrow} - \mu_H^{\downarrow} = \mu_C^{\downarrow} - \mu_C^{\uparrow} = e\left(S^{\uparrow} - S^{\downarrow}\right)\frac{\Delta T}{2} = eV_s \tag{3}$$

where V_s is defined as spin voltage; thus:

$$\frac{V_s}{\Delta T} = \frac{1}{2}\left(S^{\uparrow} - S^{\downarrow}\right) \tag{4}$$

That is, (half) the Seebeck difference of the two spin channels corresponds to the spin voltage generated at the two ends by a temperature difference of 1 K.

The thermal-to-spin voltage conversion occurring in magnetic conductors is usually referred to as spin-polarized Seebeck effect, to be distinguished from the spin-Seebeck effect observed in insulators, which instead originates from magnons. After the seminal work by Uchida *ed al*.[57] which started the spin-caloritronic rush by revealing the spin-Seebeck effect in ferromagnetic $Ni_{81}Fe_{19}$ films, similar observations have been reported for FM/non magnetic junctions,[58] magnetic semiconducting GaMnAs,[59,60] magnetic insulating $LaY_2Fe_5O_{12}$,[61–63] FM/Si magnetic tunnel junctions,[64] FM/NM/FM spin valves;[65,66] unexpectedly, the effect was even observed in non-magnetic InSb, owed to the interplay of phonon-drag and spin-orbit coupling.[67] In practice, these observations are always carried out in devices where the thermoelectric material is interfaced with another material with spin-current conversion capability; in this way, V_s gives rise to a spin current across the junction which is eventually converted to charge current by Edelstein or spin-Hall effect; in Fig.4c this spin-caloritronic architecture is adapted to our 2DEG case.

In Figure 4d we display results for spin-polarization vs charge density, obtained using an effective mass model of the 2DEG band structure. The spin-polarization values are rather close to those extracted by the calculated FS areas, attesting the substantial soundness of our predictions. For T < 50 K, the spin-polarization is barely dependent on *T*, and remains close to 100% up to a maximum density $n \sim 2\times10^{13}$ cm^{-2}, i.e. at low *T* the system is half-metallic. Above this threshold density, the minority channel starts to be significantly populated since ε_F rises above the minority band bottom, and the spin polarization progressively fades. At room T, the spin-polarization is still quite large (~95%) for densities lower than $n \sim 10^{13}$ cm^{-2}; as *n* rises further, thermal excitations redistribute the carriers to higher energies, thus re-equilibrating the spin channel occupancies. For $n = 8.5\times10^{13}$ cm^{-2}, that is the charge density of the unperturbed 2DEG for the 4 LAO layer interface, we obtain 40% and 36% spin-polarization at low *T* and room-*T*, respectively.

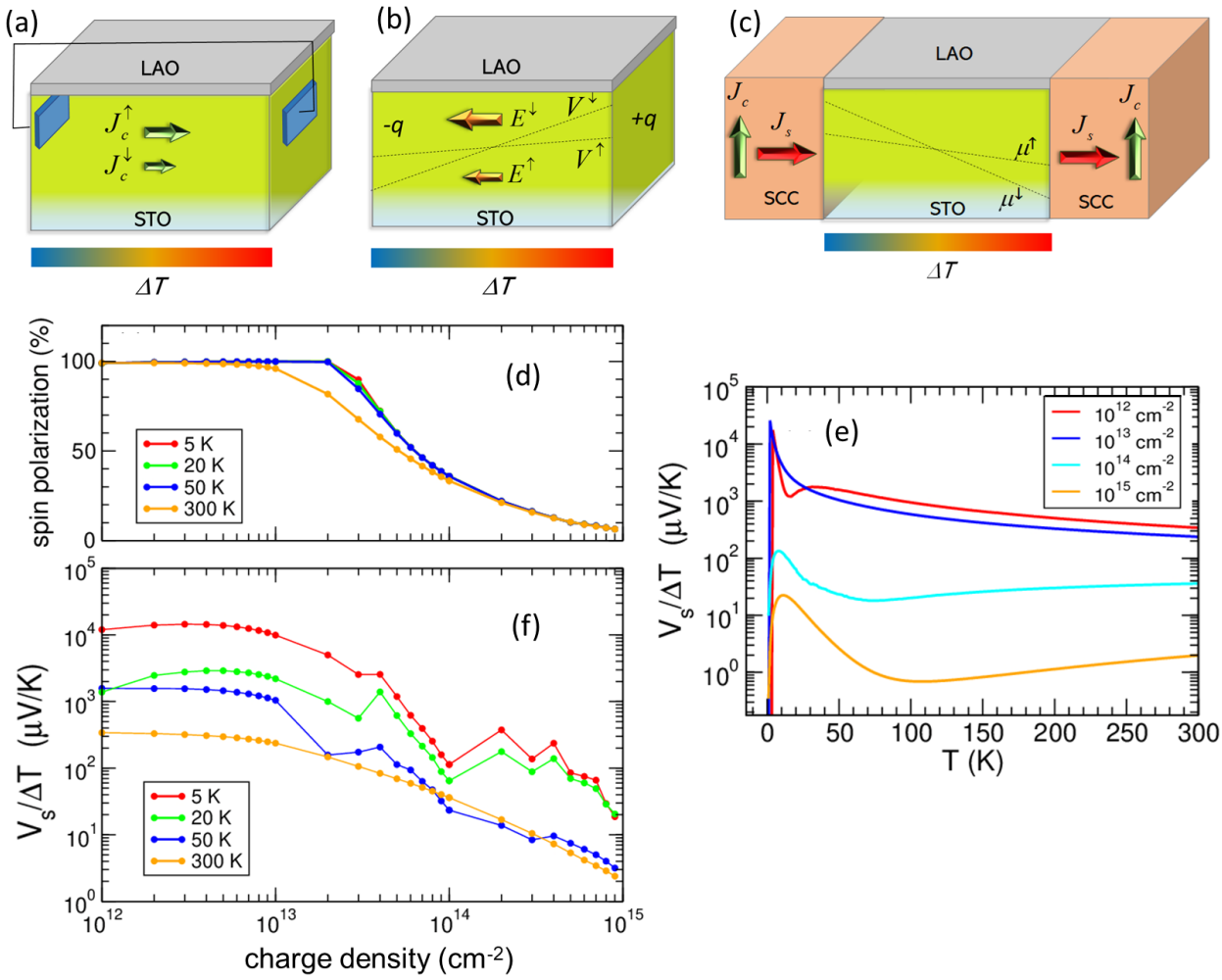

Figure 4: a): sketch of the 2DEG behavior in STO/ETO/LAO in closed-circuit condition: under an applied temperature gradient, up-spin and down-spin electrons flow from the hot side (right) to the cold side (left); the conventional currents $J_c^{\uparrow\downarrow}$ flow to the opposite verse. b): same sketch in open-circuit condition: an excess of positive and negative charge is accumulated at the hot and cold end, respectively; a potential bias $V^{\uparrow\downarrow}$, and an effective field $E^{\uparrow\downarrow}$ different for up-spin and down-spin carriers, are generated across the bar. The bias is larger for the less populated channel (down-spin in our convention). c): the 2DEG is put in contact with a material having spin-charge conversion (SCC) capabilities, e.g. by Rashba-Edelstein or spin-Hall effect. The chemical potential disalignment $\mu^{\uparrow}$ - $\mu^{\downarrow}$ on each of the two ends generate spin currents J_s through the SCC materials and in turn charge currents J_c in the orthogonal direction. d) spin-polarization fraction vs n for different T, indicated by the color legend. e) spin-voltage V_s to ΔT ratio (Eq.4). Notice that $S^{\uparrow\downarrow}$ are negative for both spin channels but $S^{\downarrow}$ is larger in magnitude, thus V_s is positive at any T and charge density. f) spin voltage vs T for different n values, indicated in the legend.

In the high density limit (n > 10^{14} cm^{-2}) the T-dependence vanishes, as both channels are substantially occupied, and thermal excitations do not alter anymore their relative population. For n ~ 3×10^{14} cm^{-2}, corresponding to half-electron charge per (1x1) unit interface, the spin-polarization is reduced to 16%, and for the highly degenerate n ~ 10^{15} cm^{-2} limit, the magnetization is almost wiped out.

In Figures 4e we report the spin voltage to ΔT ratio (Eq. 4) vs T; since $S^{\uparrow,\downarrow}$ are both negative and $S^{\downarrow}$ is larger in magnitude, $V_s/\Delta T$ is positive at any T and n. In the low-density regime ($n \sim 10^{12}$ -10^{13} cm^{-2}) $V_s/\Delta T$ is huge (~1-10 mV/K) in correspondence of the phonon-drag peak, and quite large (~0.2-0.4 mV/K) even at room T. In fact, for these low densities the spin-polarization is large at any temperature, but we should consider that the FM order in STO/ETO/LAO is only observed at low T. In Figure 4f we display $V_s/\Delta T$ vs n, for several fixed T; it is interesting noticing that at low T the spin voltage shows a sawtooth-like behavior, due to the abrupt change in population associated to the ε_F crossing of an increasing number of bands. This behavior is progressively smoothened for increasing T, and disappears at room T. At T=5 K the values of $V_s/\Delta T$ are remarkably large across the entire charge density range, e.g. for the unbiased density $n = 8\times10^{13}$ cm^{-2} we obtain $V_s/\Delta T$ ~0.8 mV/K. For the 2-ETO case (discussed in the S.I.) we find a qualitatively similar behavior. As expected, the spin-polarization is further enhanced, since spin-splitting involves two layers. However, the difference is only marked for densities $n \sim 10^{14}$ cm^{-2} or higher, while in the low-density regime, where the thermal-spin conversion process is mostly effective, spin-polarization reaches 100% for both the structures; this leads to similar spin voltages in this charge density range and in turn similar thermal-spin conversion capabilities.

We notice that our spin voltage values are significantly larger than those reported in literature for prototypical spin-caloritronic materials, ranging from nV/K to μV/K.[57–67] However, a direct comparison of our results with the experiments is complicated by the presence of some additional ingredients: the voltages measured in devices include conversion factors such as the spin-Hall angle and the spin injection efficiency across the interface which can downscale the genuine spin voltage proper of the thermoelectric material; furthermore, measurements are typically done over samples longer than the spin diffusion length, which is not considered in

our treatment. Thus, it is safe to take our estimate as an ideal upper limit of the actual material performance in devices.

In summary, in this work we propose the ultra-thin 2DEG spontaneously formed at the STO/ETO/LAO interface as a system with thermal-spin conversion capability. We gave evidence that the uneven population of the two spin channels, associated to the good electron mobility and the giant, phonon-drag derived Seebeck coefficient of the 2DEG, determines a strong spin-polarized Seebeck effect. A crucial role to the aim is played by the 2D space confinement, which can be controlled by field effect in order to consistently enhances both spin-polarization and phonon-drag contribution to thermopower. The combination of these two ingredients is instrumental to produce spin voltages which, in the ideal condition of discardable spin-flip rate, can be as large as ~1-10 mV/K at low T. Our findings configure the possibility to exploit this interface for the implementation of spin-caloritronic devices operated by field effect.

COMPUTATIONAL METHODS

Ab-initio Density Functional Theory (DFT) band structure calculations are done using the VASP code,[68] within projected augmented wave (PAW) basis set[69] and 550 eV cut-off energy. We used the GGA+U energy functional,[70,71] with U= 7.5 eV and 4.0 eV for Eu *4*f and Ti *3d* states, respectively, consistently with previous works where these values were shown to give substantial agreement with photoemission measurements.[21,27] For BZ averages, large 20×20×1 Monkhorst-Pack meshes were used; the atomic positions were fully relaxed up to a force threshold of 1 meV/Å. For the calculation of transport and thermoelectric, we carried out Bloch-Boltzmann calculations[48,49] based on relaxation-time approximation and parabolic band modelling, implemented in home-made codes. Carrier scattering includes electron-impurity scattering according to Brooks-Herring formula, the electron-acoustic phonon scattering in the deformation potential approximation, and the electron-optical phonon scattering as described

by the Fletcher-Butcher formulation.[50,72] Finally, the phonon drag term is implemented according to the Bailey formalism.[55,56]

ASSOCIATED CONTENT

Supporting Information.

AUTHOR INFORMATION

Corresponding Author

Alessio Filippetti

E-mail: alessio.filippetti@dsf.unica.it

ORCID: orcid.org/0000-0002-9144-7005

Author Contributions

The manuscript was written through contributions of all authors.

Notes

The authors declare no competing financial interest.

ACKNOWLEDGMENTS

Work supported by project PRIN 2017 “TOPSPIN”, funded by Italian Ministry of University and Research (MIUR),

REFERENCES

(1) Ohtomo, A.; Hwang, H. Y. A High-Mobility Electron Gas at the LaAlO3/SrTiO3 Heterointerface. *Nature* **2004**, *427* (6973), 423–426.

(2) Katsufuji, T.; Takagi, H. Coupling between Magnetism and Dielectric Properties in Quantum Paraelectric EuTiO 3. *Phys. Rev. B* **2001**, *64* (5), 054415.

(3) Fennie, C. J.; Rabe, K. M. Magnetic and Electric Phase Control in Epitaxial EuTiO 3 from First Principles. *Phys. Rev. Lett.* **2006**, *97* (26), 267602.

(4) Kamba, S.; Nuzhnyy, D.; Vaněk, P.; Savinov, M.; Knížek, K.; Shen, Z.; Šantavá, E.; Maca, K.; Sadowski, M.; Petzelt, J. Magnetodielectric Effect and Optic Soft Mode

Behaviour in Quantum Paraelectric EuTiO $_3$ Ceramics. *Europhys. Lett. EPL* **2007**, *80* (2), 27002.
(5) Goian, V.; Kamba, S.; Hlinka, J.; Vaněk, P.; Belik, A. A.; Kolodiazhnyi, T.; Petzelt, J. Polar Phonon Mixing in Magnetoelectric EuTiO3. *Eur. Phys. J. B* **2009**, *71* (3), 429–433.
(6) Lee, J. H.; Ke, X.; Podraza, N. J.; Kourkoutis, L. F.; Heeg, T.; Roeckerath, M.; Freeland, J. W.; Fennie, C. J.; Schubert, J.; Muller, D. A.; Schiffer, P.; Schlom, D. G. Optical Band Gap and Magnetic Properties of Unstrained EuTiO3 Films. *Appl. Phys. Lett.* **2009**, *94* (21), 212509.
(7) Lee, J. H.; Fang, L.; Vlahos, E.; Ke, X.; Jung, Y. W.; Kourkoutis, L. F.; Kim, J.-W.; Ryan, P. J.; Heeg, T.; Roeckerath, M.; Goian, V.; Bernhagen, M.; Uecker, R.; Hammel, P. C.; Rabe, K. M.; Kamba, S.; Schubert, J.; Freeland, J. W.; Muller, D. A.; Fennie, C. J.; Schiffer, P.; Gopalan, V.; Johnston-Halperin, E.; Schlom, D. G. A Strong Ferroelectric Ferromagnet Created by Means of Spin–Lattice Coupling. *Nature* **2010**, *466* (7309), 954–958.
(8) Ellis, D. S.; Uchiyama, H.; Tsutsui, S.; Sugimoto, K.; Kato, K.; Ishikawa, D.; Baron, A. Q. R. Phonon Softening and Dispersion in EuTiO 3. *Phys. Rev. B* **2012**, *86* (22), 220301.
(9) Kamba, S.; Goian, V.; Orlita, M.; Nuzhnyy, D.; Lee, J. H.; Schlom, D. G.; Rushchanskii, K. Z.; Ležaić, M.; Birol, T.; Fennie, C. J.; Gemeiner, P.; Dkhil, B.; Bovtun, V.; Kempa, M.; Hlinka, J.; Petzelt, J. Magnetodielectric Effect and Phonon Properties of Compressively Strained EuTiO 3 Thin Films Deposited on (001)(LaAlO 3) 0.29 -(SrAl 1 / 2 Ta 1 / 2 O 3) 0.71. *Phys. Rev. B* **2012**, *85* (9), 094435.
(10) Ryan, P. J.; Kim, J.-W.; Birol, T.; Thompson, P.; Lee, J.-H.; Ke, X.; Normile, P. S.; Karapetrova, E.; Schiffer, P.; Brown, S. D.; Fennie, C. J.; Schlom, D. G. Reversible Control of Magnetic Interactions by Electric Field in a Single-Phase Material. *Nat. Commun.* **2013**, *4* (1), 1334.
(11) Reuvekamp, P. G.; Kremer, R. K.; Köhler, J.; Bussmann-Holder, A. Spin-Lattice Coupling Induced Crossover from Negative to Positive Magnetostriction in EuTiO 3. *Phys. Rev. B* **2014**, *90* (9), 094420.
(12) Reuvekamp, P.; Caslin, K.; Guguchia, Z.; Keller, H.; Kremer, R. K.; Simon, A.; Köhler, J.; Bussmann-Holder, A. Tiny Cause with Huge Impact: Polar Instability through Strong Magneto-Electric-Elastic Coupling in Bulk EuTiO $_3$. *J. Phys. Condens. Matter* **2015**, *27* (26), 262201.
(13) Bussmann-Holder, A.; Köhler, J. Revisiting the Fascinating Properties of EuTiO 3 and Its Mixed Crystals with SrTiO 3 : Possible Candidates for Novel Functionalities. *J. Phys. Chem. Solids* **2015**, *84*, 2–12.
(14) Bussmann-Holder, A.; Roleder, K.; Stuhlhofer, B.; Logvenov, G.; Lazar, I.; Soszyński, A.; Koperski, J.; Simon, A.; Köhler, J. Transparent EuTiO3 Films: A Possible Two-Dimensional Magneto-Optical Device. *Sci. Rep.* **2017**, *7* (1), 40621.
(15) Lin, Y.; Choi, E.-M.; Lu, P.; Sun, X.; Wu, R.; Yun, C.; Zhu, B.; Wang, H.; Li, W.; Maity, T.; MacManus-Driscoll, J. Vertical Strain-Driven Antiferromagnetic to Ferromagnetic Phase Transition in EuTiO $_3$ Nanocomposite Thin Films. *ACS Appl. Mater. Interfaces* **2020**, *12* (7), 8513–8521.
(16) Ryan, P. J.; Sterbinsky, G. E.; Choi, Y.; Woicik, J. C.; Zhu, L.; Jiang, J. S.; Lee, J.-H.; Schlom, D. G.; Birol, T.; Brown, S. D.; Thompson, P. B. J.; Normile, P. S.; Lang, J.; Kim, J.-W. Multiferroic Behavior in EuTi O 3 Films Constrained by Symmetry. *Phys. Rev. B* **2020**, *101* (18), 180409.
(17) Akamatsu, H.; Kumagai, Y.; Oba, F.; Fujita, K.; Murakami, H.; Tanaka, K.; Tanaka, I. Antiferromagnetic Superexchange via 3 d States of Titanium in EuTiO 3 as Seen from Hybrid Hartree-Fock Density Functional Calculations. *Phys. Rev. B* **2011**, *83* (21), 214421.

(18) Kolodiazhnyi, T.; Valant, M.; Williams, J. R.; Bugnet, M.; Botton, G. A.; Ohashi, N.; Sakka, Y. Evidence of Eu $^{2+}$ 4 *f* Electrons in the Valence Band Spectra of EuTiO $_3$ and EuZrO $_3$. *J. Appl. Phys.* **2012**, *112* (8), 083719.
(19) Birol, T.; Fennie, C. J. Origin of Giant Spin-Lattice Coupling and the Suppression of Ferroelectricity in EuTiO 3 from First Principles. *Phys. Rev. B* **2013**, *88* (9), 094103.
(20) Gui, Z.; Janotti, A. Carrier-Density-Induced Ferromagnetism in EuTiO 3 Bulk and Heterostructures. *Phys. Rev. Lett.* **2019**, *123* (12), 127201.
(21) Wadhwa, P.; Bosin, A.; Filippetti, A. Giant Spin-Dependent Seebeck Effect from Fully Spin-Polarized Carriers in n-Doped EuTiO3: A Prototype Material for Spin-Caloritronic Applications. *J Mater Chem A* **2023**.
(22) Katsufuji, T.; Tokura, Y. Transport and Magnetic Properties of a Ferromagnetic Metal: Eu 1 − x R x TiO 3. *Phys. Rev. B* **1999**, *60* (22), R15021–R15023.
(23) Takahashi, K. S.; Onoda, M.; Kawasaki, M.; Nagaosa, N.; Tokura, Y. Control of the Anomalous Hall Effect by Doping in Eu 1 − x La x TiO 3 Thin Films. *Phys. Rev. Lett.* **2009**, *103* (5), 057204.
(24) Li, L.; Zhou, H.; Yan, J.; Mandrus, D.; Keppens, V. Research Update: Magnetic Phase Diagram of EuTi $_{1-x}$ *B* $_x$ O $_3$ (*B* = Zr, Nb). *APL Mater.* **2014**, *2* (11), 110701.
(25) Li, L.; Morris, J. R.; Koehler, M. R.; Dun, Z.; Zhou, H.; Yan, J.; Mandrus, D.; Keppens, V. Structural and Magnetic Phase Transitions in EuTi 1 − x Nb x O 3. *Phys. Rev. B* **2015**, *92* (2), 024109.
(26) Yamamoto, T.; Yoshii, R.; Bouilly, G.; Kobayashi, Y.; Fujita, K.; Kususe, Y.; Matsushita, Y.; Tanaka, K.; Kageyama, H. An Antiferro-to-Ferromagnetic Transition in EuTiO $_{3-x}$ H $_x$ Induced by Hydride Substitution. *Inorg. Chem.* **2015**, *54* (4), 1501–1507.
(27) Di Capua, R.; Verma, M.; Radović, M.; Plumb, N. C.; Dil, J. H.; Ristić, Z.; Guedes, E. B.; De Luca, G. M.; Preziosi, D.; Wang, Z.; Weber, A. P.; Pentcheva, R.; Salluzzo, M. Two-Dimensional Electron Gas at the (001) Surface of Ferromagnetic EuTiO 3. *Phys. Rev. Res.* **2021**, *3* (4), L042038.
(28) De Luca, G. M.; Di Capua, R.; Di Gennaro, E.; Granozio, F. M.; Stornaiuolo, D.; Salluzzo, M.; Gadaleta, A.; Pallecchi, I.; Marrè, D.; Piamonteze, C.; Radovic, M.; Ristic, Z.; Rusponi, S. Transport Properties of a Quasi-Two-Dimensional Electron System Formed in LaAlO 3 / EuTiO 3 / SrTiO 3 Heterostructures. *Phys. Rev. B* **2014**, *89* (22), 224413.
(29) Stornaiuolo, D.; Cantoni, C.; De Luca, G. M.; Di Capua, R.; Di. Gennaro, E.; Ghiringhelli, G.; Jouault, B.; Marrè, D.; Massarotti, D.; Miletto Granozio, F.; Pallecchi, I.; Piamonteze, C.; Rusponi, S.; Tafuri, F.; Salluzzo, M. Tunable Spin Polarization and Superconductivity in Engineered Oxide Interfaces. *Nat. Mater.* **2016**, *15* (3), 278–283.
(30) Stornaiuolo, D.; Jouault, B.; Di Gennaro, E.; Sambri, A.; D'Antuono, M.; Massarotti, D.; Granozio, F. M.; Di Capua, R.; De Luca, G. M.; Pepe, G. P.; Tafuri, F.; Salluzzo, M. Interplay between Spin-Orbit Coupling and Ferromagnetism in Magnetotransport Properties of a Spin-Polarized Oxide Two-Dimensional Electron System. *Phys. Rev. B* **2018**, *98* (7), 075409.
(31) Di Capua, R.; Verma, M.; Radovic, M.; Strocov, V. N.; Piamonteze, C.; Guedes, E. B.; Plumb, N. C.; Chen, Y.; D'Antuono, M.; De Luca, G. M.; Di Gennaro, E.; Stornaiuolo, D.; Preziosi, D.; Jouault, B.; Miletto Granozio, F.; Sambri, A.; Pentcheva, R.; Ghiringhelli, G.; Salluzzo, M. Orbital Selective Switching of Ferromagnetism in an Oxide Quasi Two-Dimensional Electron Gas. *Npj Quantum Mater.* **2022**, *7* (1), 41.
(32) Maruhashi, K.; Takahashi, K. S.; Bahramy, M. S.; Shimizu, S.; Kurihara, R.; Miyake, A.; Tokunaga, M.; Tokura, Y.; Kawasaki, M. Anisotropic Quantum Transport through a Single Spin Channel in the Magnetic Semiconductor EuTiO $_3$. *Adv. Mater.* **2020**, *32* (24), 1908315.

(33) Bauer, G. E. W.; Saitoh, E.; van Wees, B. J. Spin Caloritronics. *Nat. Mater.* **2012**, *11* (5), 391–399.
(34) Boona, S. R.; Myers, R. C.; Heremans, J. P. Spin Caloritronics. *Energy Environ. Sci.* **2014**, *7* (3), 885.
(35) Yu, H.; Brechet, S. D.; Ansermet, J.-P. Spin Caloritronics, Origin and Outlook. *Phys. Lett. A* **2017**, *381* (9), 825–837.
(36) Uchida, K. Transport Phenomena in Spin Caloritronics. *Proc. Jpn. Acad. Ser. B* **2021**, *97* (2), 69–88.
(37) Ohta, H.; Kim, S.; Mune, Y.; Mizoguchi, T.; Nomura, K.; Ohta, S.; Nomura, T.; Nakanishi, Y.; Ikuhara, Y.; Hirano, M.; Hosono, H.; Koumoto, K. Giant Thermoelectric Seebeck Coefficient of a Two-Dimensional Electron Gas in SrTiO3. *Nat. Mater.* **2007**, *6* (2), 129–134.
(38) Ohta, H. Thermoelectrics Based on Strontium Titanate. *Mater. Today* **2007**, *10* (10), 44–49.
(39) Filippetti, A.; Delugas, P.; Verstraete, M. J.; Pallecchi, I.; Gadaleta, A.; Marré, D.; Li, D. F.; Gariglio, S.; Fiorentini, V. Thermopower in Oxide Heterostructures: The Importance of Being Multiple-Band Conductors. *Phys. Rev. B* **2012**, *86* (19), 195301.
(40) Pallecchi, I.; Telesio, F.; Li, D.; Fête, A.; Gariglio, S.; Triscone, J.-M.; Filippetti, A.; Delugas, P.; Fiorentini, V.; Marré, D. Giant Oscillating Thermopower at Oxide Interfaces. *Nat. Commun.* **2015**, *6* (1), 6678.
(41) Pallecchi, I.; Telesio, F.; Marré, D.; Li, D.; Gariglio, S.; Triscone, J.-M.; Filippetti, A. Large Phonon-Drag Enhancement Induced by Narrow Quantum Confinement at the LaAlO 3 / SrTiO 3 Interface. *Phys. Rev. B* **2016**, *93* (19), 195309.
(42) Reyren, N.; Thiel, S.; Caviglia, A. D.; Kourkoutis, L. F.; Hammerl, G.; Richter, C.; Schneider, C. W.; Kopp, T.; Rüetschi, A.-S.; Jaccard, D.; Gabay, M.; Muller, D. A.; Triscone, J.-M.; Mannhart, J. Superconducting Interfaces Between Insulating Oxides. *Science* **2007**, *317* (5842), 1196–1199.
(43) Caviglia, A. D.; Gariglio, S.; Reyren, N.; Jaccard, D.; Schneider, T.; Gabay, M.; Thiel, S.; Hammerl, G.; Mannhart, J.; Triscone, J.-M. Electric Field Control of the LaAlO3/SrTiO3 Interface Ground State. *Nature* **2008**, *456* (7222), 624–627.
(44) Caviglia, A. D.; Gabay, M.; Gariglio, S.; Reyren, N.; Cancellieri, C.; Triscone, J.-M. Tunable Rashba Spin-Orbit Interaction at Oxide Interfaces. *Phys. Rev. Lett.* **2010**, *104* (12), 126803.
(45) Delugas, P.; Filippetti, A.; Fiorentini, V.; Bilc, D. I.; Fontaine, D.; Ghosez, P. Spontaneous 2-Dimensional Carrier Confinement at the n -Type SrTiO 3 / LaAlO 3 Interface. *Phys. Rev. Lett.* **2011**, *106* (16), 166807.
(46) Delugas, P.; Filippetti, A.; Gadaleta, A.; Pallecchi, I.; Marré, D.; Fiorentini, V. Large Band Offset as Driving Force of Two-Dimensional Electron Confinement: The Case of SrTiO 3 /SrZrO 3 Interface. *Phys. Rev. B* **2013**, *88* (11), 115304.
(47) Delugas, P.; Fiorentini, V.; Mattoni, A.; Filippetti, A. Intrinsic Origin of Two-Dimensional Electron Gas at the (001) Surface of SrTiO 3. *Phys. Rev. B* **2015**, *91* (11), 115315.
(48) P. B. Allen, Boltzmann Theory and Resistivity of Metals, in: Chelikowsky, J. R., Louie, S. G., (Eds.), Quantum Theory of Real Materials, Kluwer, Boston, **1996**, pp. 219–250
(49) Madsen, G. K. H.; Singh, D. J. BoltzTraP. A Code for Calculating Band-Structure Dependent Quantities. *Comput. Phys. Commun.* **2006**, *175* (1), 67–71.
(50) Ridley, B. K. *Quantum Processes in Semiconductors*, 2nd ed.; Clarendon Press ; Oxford University Press: Oxford : New York, 1988.
(51) Puggioni, D.; Filippetti, A.; Fiorentini, V. Ordering and Multiple Phase Transitions in Ultrathin Nickelate Superlattices. *Phys. Rev. B* **2012**, *86* (19), 195132.

(52) Delugas, P.; Filippetti, A.; Verstraete, M. J.; Pallecchi, I.; Marré, D.; Fiorentini, V. Doping-Induced Dimensional Crossover and Thermopower Burst in Nb-Doped SrTiO 3 Superlattices. *Phys. Rev. B* **2013**, *88* (4), 045310.
(53) Tsaousidou, M.; Butcher, P. N.; Triberis, G. P. Fundamental Relationship between the Herring and Cantrell-Butcher Formulas for the Phonon-Drag Thermopower of Two-Dimensional Electron and Hole Gases. *Phys. Rev. B* **2001**, *64* (16), 165304.
(54) Tsaousidou, M. Ultra-Low Acoustic-Phonon-Limited Mobility and Giant Phonon-Drag Thermopower in MgZnO/ZnO Heterostructures: Ultra-Low Acoustic-Phonon-Limited Mobility and Giant Phonon-Drag Thermopower in MgZnO/ZnO Heterostructures. *Phys. Status Solidi RRL - Rapid Res. Lett.* **2013**, *7* (8), 554–557.
(55) Bailyn, M. Phonon-Drag Part of the Thermoelectric Power in Metals. *Phys. Rev.* **1967**, *157* (3), 480–485.
(56) Cantrell, D. G.; Butcher, P. N. A Calculation of the Phonon Drag Contribution to Thermopower in Two Dimensional Systems. *J. Phys. C Solid State Phys.* **1986**, *19* (20), L429–L432.
(57) Uchida, K.; Takahashi, S.; Harii, K.; Ieda, J.; Koshibae, W.; Ando, K.; Maekawa, S.; Saitoh, E. Observation of the Spin Seebeck Effect. *Nature* **2008**, *455* (7214), 778–781.
(58) Slachter, A.; Bakker, F. L.; Adam, J.-P.; van Wees, B. J. Thermally Driven Spin Injection from a Ferromagnet into a Non-Magnetic Metal. *Nat. Phys.* **2010**, *6* (11), 879–882.
(59) Jaworski, C. M.; Yang, J.; Mack, S.; Awschalom, D. D.; Heremans, J. P.; Myers, R. C. Observation of the Spin-Seebeck Effect in a Ferromagnetic Semiconductor. *Nat. Mater.* **2010**, *9* (11), 898–903.
(60) Jaworski, C. M.; Yang, J.; Mack, S.; Awschalom, D. D.; Myers, R. C.; Heremans, J. P. Spin-Seebeck Effect: A Phonon Driven Spin Distribution. *Phys. Rev. Lett.* **2011**, *106* (18), 186601.
(61) Uchida, K.; Xiao, J.; Adachi, H.; Ohe, J.; Takahashi, S.; Ieda, J.; Ota, T.; Kajiwara, Y.; Umezawa, H.; Kawai, H.; Bauer, G. E. W.; Maekawa, S.; Saitoh, E. Spin Seebeck Insulator. *Nat. Mater.* **2010**, *9* (11), 894–897.
(62) Adachi, H.; Ohe, J.; Takahashi, S.; Maekawa, S. Linear-Response Theory of Spin Seebeck Effect in Ferromagnetic Insulators. *Phys. Rev. B* **2011**, *83* (9), 094410.
(63) Adachi, H.; Uchida, K.; Saitoh, E.; Ohe, J.; Takahashi, S.; Maekawa, S. Gigantic Enhancement of Spin Seebeck Effect by Phonon Drag. *Appl. Phys. Lett.* **2010**, *97* (25), 252506.
(64) Le Breton, J.-C.; Sharma, S.; Saito, H.; Yuasa, S.; Jansen, R. Thermal Spin Current from a Ferromagnet to Silicon by Seebeck Spin Tunnelling. *Nature* **2011**, *475* (7354), 82–85.
(65) Flipse, J.; Bakker, F. L.; Slachter, A.; Dejene, F. K.; van Wees, B. J. Direct Observation of the Spin-Dependent Peltier Effect. *Nat. Nanotechnol.* **2012**, *7* (3), 166–168.
(66) Dejene, F. K.; Flipse, J.; Bauer, G. E. W.; van Wees, B. J. Spin Heat Accumulation and Spin-Dependent Temperatures in Nanopillar Spin Valves. *Nat. Phys.* **2013**, *9* (10), 636–639.
(67) Jaworski, C. M.; Myers, R. C.; Johnston-Halperin, E.; Heremans, J. P. Giant Spin Seebeck Effect in a Non-Magnetic Material. *Nature* **2012**, *487* (7406), 210–213.
(68) Kresse, G.; Furthmüller, J. Efficient Iterative Schemes for *Ab Initio* Total-Energy Calculations Using a Plane-Wave Basis Set. *Phys. Rev. B* **1996**, *54* (16), 11169–11186.
(69) Kresse, G.; Joubert, D. From Ultrasoft Pseudopotentials to the Projector Augmented-Wave Method. *Phys. Rev. B* **1999**, *59* (3), 1758–1775.
(70) Perdew, J. P.; Burke, K.; Ernzerhof, M. Generalized Gradient Approximation Made Simple. *Phys. Rev. Lett.* **1996**, *77* (18), 3865–3868.
(71) Anisimov, V. I.; Zaanen, J.; Andersen, O. K. Band Theory and Mott Insulators: Hubbard *U* Instead of Stoner *I*. *Phys. Rev. B* **1991**, *44* (3), 943–954.

(72) Fletcher, K.; Butcher, P. N. Solution of the Boltzmann Equation in Ellipsoidal Valleys with Application to the Valleys of GaAs and GaP. *J. Phys. C Solid State Phys.* **1973**, *6* (6), 976–996.